

Analysis of dense-medium light scattering with applications to corneal tissue: experiments and Monte Carlo simulations

K. B. Kim, L. M. Shanyfelt, and D. W. Hahn

Department of Mechanical and Aerospace Engineering, University of Florida, Gainesville, Florida 32611

Received December 22, 2004; revised manuscript received May 13, 2005; accepted June 8, 2005

Dense-medium scattering is explored in the context of providing a quantitative measurement of turbidity, with specific application to corneal haze. A multiple-wavelength scattering technique is proposed to make use of two-color scattering response ratios, thereby providing a means for data normalization. A combination of measurements and simulations are reported to assess this technique, including light-scattering experiments for a range of polystyrene suspensions. Monte Carlo (MC) simulations were performed using a multiple-scattering algorithm based on full Mie scattering theory. The simulations were in excellent agreement with the polystyrene suspension experiments, thereby validating the MC model. The MC model was then used to simulate multiwavelength scattering in a corneal tissue model. Overall, the proposed multiwavelength scattering technique appears to be a feasible approach to quantify dense-medium scattering such as the manifestation of corneal haze, although more complex modeling of keratocyte scattering, and animal studies, are necessary.

© 2006 Optical Society of America

OCIS codes: 120.3890, 170.3660, 170.4460, 170.7050, 290.4210.

1. INTRODUCTION

In general, corneal transparency and visual acuity are dependent on the unique matrix of collagen fibrils and proteoglycans that constitutes the corneal stroma. Keratocytes, fibroblastlike cells, are also present in the corneal stroma and play several important roles in the dynamics of this tissue system. Keratocytes function in the processes that maintain corneal transparency by regulating collagen fibril size and spacing within the proteoglycan matrix.^{1,2} Perturbations to any of the corneal constituent structures may remodel the corneal stroma and consequently lead to reductions in corneal transparency, loss of visual acuity, and the presence of corneal haze. Such events may be the result of photochemical processes resulting from refractive surgery, for example, photorefractive keratectomy (PRK) and laser-assisted *in situ* keratomileusis (LASIK), or may result from a number of corneal diseases (e.g., herpetic keratitis, corneal ulceration, and corneal dystrophies) or corneal trauma and subsequent wound healing.

Corneal haze is manifest as the redirection of incident light out of the path of the incident ray by the presence of biological structures not associated with the normal corneal matrix, such as activated keratocytes.³⁻⁵ Such a redirection or redistribution of light by small objects (i.e., heterogeneities) is by definition a light-scattering process. Such an observation is consistent with a number of reported studies that utilize various light-scattering approaches as a means to quantify corneal haze. Clinical and laboratory studies may benefit from quantitative measurements of dense-medium scattering to better assess the statistical relevance of corneal haze manifestation and control under different conditions. Although the use of light scattering as a means of corneal haze assess-

ment appears to be a rather straightforward approach, the development of a robust implementation has not been forthcoming.

2. LIGHT-SCATTERING BACKGROUND

A. Corneal Haze Assessment

Only a few techniques of clinical haze assessment have been proposed, which are described in this brief review. Generally, these techniques fall into the broad categories of scattering-based measurements and confocal microscopy. Several early studies used polychromatic light (i.e., white light) from slit lamps or similar sources to assess the state of corneal haze. Lohmann *et al.* utilized polarizers in an attempt to discriminate between true corneal scattering and reflectance from the corneal surface.⁶ While their approach did demonstrate a response of the scattering signal to corneal haze, the measurements were relative to specific patients, precision was limited, and no absolute scale was applicable for patient-to-patient comparisons. A similar technique, referred to by the investigators as scatterometry, has been reported and used for a number of corneal ablation studies.⁷⁻⁹ The device used a modified slit lamp to illuminate the corneal surface and a photomultiplier detector to record collected scattered light. All corneal haze measurements were referenced to an optical grade standard, and a scattering index was used to normalize the signals to an average of 13 normal eyes. Accuracy was a significant limitation of this scattering metric, notably with modest postoperative haze formation following PRK.

Andrade *et al.* investigated corneal clarity using a commercially available opacity lensometer, a device that measures 700 nm-light scattered and/or reflected out of the

eye.¹⁰ The researchers concluded that the approach lacked sufficient sensitivity and failed to distinguish between corneas with different amounts of haze. While all of these approaches demonstrate the utility of the corneal scattering function as a metric for haze, issues such as signal normalization to a common scale, precision and reproducibility, and discrimination of true corneal scattering from surface reflectance all present significant problems.

In recent years, perhaps the most widely reported instrument for corneal haze assessment is based on the techniques of confocal microscopy and digital image analysis to quantify corneal haze with excellent spatial resolution (both depth and x - y directions).^{11,12} A number of studies by the group who carried out this research have utilized the confocal instrument, including recent studies of stromal wound healing and haze development.^{4,13} Although perhaps the most successful of the haze assessment techniques, the confocal instrument does not provide high precision nor an absolute measure of haze; hence, the device, as noted by the researchers, is applicable only in assessing visual outcomes in individual cases. Additional issues are the overall complexity and cost of the instrument, making duplication infeasible for many research projects, animal studies, or widespread clinical implementation.

B. Monte Carlo Modeling

An important step to understanding better the interactions of light with the dense medium characteristic of corneal tissue, hence a key step in efforts to quantify haze measurements, is to develop effective tools to model the light-scattering problem. To this end, Monte Carlo (MC) simulation is a powerful tool for statistical solution of complex problems such as multiple scattering in dense tissue. The MC technique has been used to study light scattering in tissue and to evaluate tissue optical properties, which is essential in biological laser applications. Wang *et al.* developed a hybrid model of MC simulation and diffusion theory to model and compute the light reflectance in semi-infinite turbid media.^{14,15} This hybrid model has not only the accuracy advantage of MC simulation, but also the computational advantage of diffusion theory, thereby overcoming the speed disadvantage of pure MC simulation and allowing better accuracy.¹⁴ The reader is referred to these sources^{14,15} for a general treatment of the MC method as applied to the general problem of tissue scattering. Another MC model of steady-state light transport in multilayered tissue was coded in American National Standards Institute (ANSI) standard C by the same research group.¹⁵ The computational results were consistent with others', while a decrease in the computational time by use of implicit photon capture was realized.

A wide range of studies have been reported that make use of MC modeling as applied to biological tissues. Key *et al.* utilized MC sampling controlled by relevant probability distributions and photon transport theory, enabling individual photons to be tracked as they moved through simulated breast tissue.¹⁶ In a study on photon migration through highly scattering inhomogeneous media, Sassaroli *et al.* showed that the temporal simulation response

for an inhomogeneous medium was faster than that for a homogeneous medium.¹⁷ Bartel *et al.* simulated polarization-dependent light scattering and propagation through highly scattering media using a MC simulation that builds a scattering event based on Mie theory, keeps track of the polarization state of individual photons, and computes two-dimensional (2D) elements of the diffuse backscattering Mueller matrix in multiple-scattering media.¹⁸ Koelink *et al.* successfully used a MC technique to verify experimental results of skin perfusion conducted by a laser Doppler blood-flow meter.¹⁹ The simulations were used for analyzing different wavelengths and optical probe geometries, and a system that could probe skin at varying depths was developed in the study.

Kienle *et al.* employed MC simulation to confirm the scattering coefficient and anisotropy factor of blood.²⁰ In addition, MC simulations have been used to solve the linear Boltzmann equation of photon transport for varying mean free paths; the results from the simulation were then compared with experimental results of a polarization-dependent scattering matrix using polystyrene (PS) latex spheres.²¹ MC simulation facilitated a better understanding of the photophysical interaction of excitation and fluorescent light in tissue, and was used by Pogue and Burke to design a tissue fluorescence probe and to confirm their experimental results.²²

3. LIGHT-SCATTERING THEORY

Light scattering is applied in this study as an analytical tool for the dense-medium scattering problem, hence formal treatment is presented in this section to provide background knowledge for the experimental measurements and the MC simulations. Light-scattering theory may be categorized in terms of two theoretical frameworks. One is the theory of Rayleigh scattering that is applicable to small, dielectric (nonabsorbing), spherical particles. The second is the theory of Mie scattering that encompasses the general spherical scattering solution (absorbing or nonabsorbing) without a particular bound on particle size. The reader is referred to three texts for a detailed treatment of both Mie and Rayleigh scattering theory.²³⁻²⁵

In the first, Mie scattering theory was applied and described in accordance with the treatment and notation of Kerker (1969).²³ In addition, to treat particles as single Mie scattering particles, several conditions must be satisfied as reported by Jones (1979).²⁶ Namely, the particle-to-particle separation must be sufficient to eliminate electrical field interactions, which is satisfied if the distance between scattering particle centers is two to three times greater than the diameter of the particles.²³ Figure 1 shows the spherical coordinate scattering geometry used for Mie light scattering for light incident on a single particle. Using this coordinate system, the scattering parameters may be defined as follows.

For each scattering angle (ϕ, θ) , the following Eqs. (1) and (2) represent the intensities of scattered radiation vertically and horizontally polarized with respect to the scattering plane, which is defined by the incident and scattered ray,

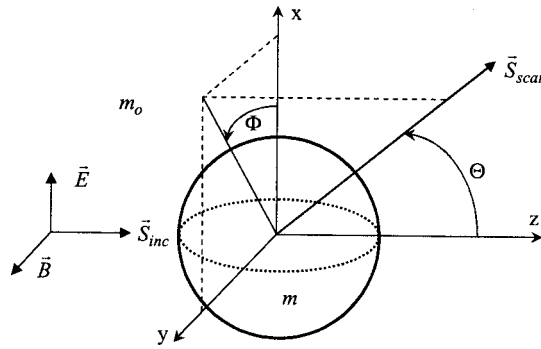


Fig. 1. Mie light scattering particle geometry in the spherical coordinate system.

$$I_{\phi} = I_0 \frac{\lambda^2}{4\pi^2 r^2} i_1 \sin^2 \phi, \quad (1)$$

$$I_{\theta} = I_0 \frac{\lambda^2}{4\pi^2 r^2} i_2 \cos^2 \phi. \quad (2)$$

Using Mie theory, the intensity functions i_1 and i_2 are complex functions of Legendre polynomials, half-integer-order Bessel functions of the first kind, and half-integer-order Hankel functions of the second kind.

The polarization-dependent differential scattering cross sections (cm^2/sr) are now defined by Eqs. (3) and (4) below, where subscript 1 refers to the polarization orientation of the incident light with respect to the scattering plane, and subscript 2 refers to the polarization orientation of the scattered light with respect to the scattering plane. Specifically, the subscripts V and H refer to the vertical polarization and the horizontal polarization states, respectively.

$$\sigma'_{VV} = \frac{\lambda^2}{4\pi^2} i_1, \quad (3)$$

$$\sigma'_{HH} = \frac{\lambda^2}{4\pi^2} i_2. \quad (4)$$

The above two equations are averaged to define the differential scattering cross section for unpolarized incident light, which is given by the relation

$$\sigma'_{scat} = \frac{\lambda^2}{8\pi^2} (i_1 + i_2). \quad (5)$$

Equations (1)–(4) may be combined to enable calculation of the scattered intensity of light in terms of the differential scattering cross sections:

$$I_{VV} = I_0 \frac{1}{r^2} \sigma'_{VV} \sin^2 \phi, \quad (6)$$

$$I_{HH} = I_0 \frac{1}{r^2} \sigma'_{HH} \cos^2 \phi, \quad (7)$$

$$I_{scat} = I_0 \frac{1}{r^2} \sigma'_{scat}. \quad (8)$$

4. EXPERIMENTAL AND COMPUTATIONAL METHODS

This paper reports on the use of a multicolor-light-scattering signal ratio to provide an accurate, precise, quantitative measurement of dense-medium scattering that may be applicable to corneal tissue. A key component is the elimination of surface reflection effects by use of a multifiber-optic probe. The current study was conducted in three parts. First, multicolor light scattering experiments were performed and analyzed using PS suspensions, designed to simulate a dense-medium scattering environment. Second, a multiple-scattering model was developed using MC simulations that was validated with the PS suspension experiments. Finally, the MC code was extended to model the corneal geometry, and was then used to optimize the multicolor scattering approach for the general problem of corneal haze.

A. Polystyrene Suspension Experiments

Light-scattering experiments were conducted using a three-color scattering system and PS suspensions with known monodisperse particle size and known particle number density. The experimental system was designed to compare the multiple-scattering intensity levels of three laser wavelengths at each of three fiber-optic collection locations. The three lasers employed were a He–Ne laser ($\lambda = 594 \text{ nm}$) and two solid-state diode lasers operating at nominal wavelengths of 532 nm and 670 nm. All wavelengths used in this study were selected based on common gas lasers (e.g., He–Ne) and diode lasers that are readily available at low or moderate cost. The total output of each laser was less than 3 mW continuous laser power.

A schematic of the experimental setup is shown in Fig. 2. The three laser beams were brought together coaxially using a series of mirrors and optical wedges, and then launched into a single 200 μm -core-diameter multimode optical fiber (coated silica, 0.22 numerical aperture). This fiber will be referred to as the illumination fiber; it functioned to introduce the three laser wavelengths into the PS suspension simultaneously as described below. The illumination fiber was mounted to a fiber holder as shown in Fig. 3. Three additional identical fibers were mounted to the fiber holder. All four fibers were mounted flush with the fiber holder surface and cemented into place on the back side. The three additional fibers, which will be re-

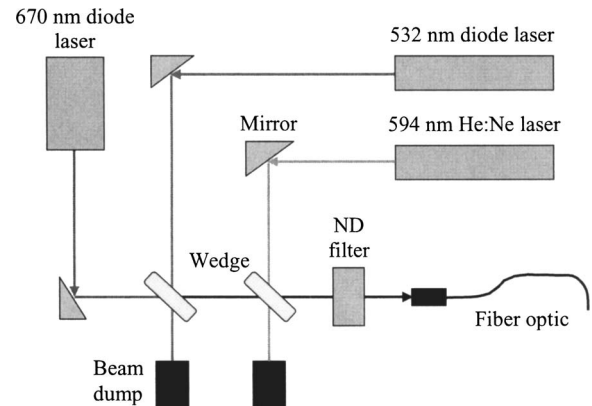


Fig. 2. Schematic of three-color wavelength optical setup.

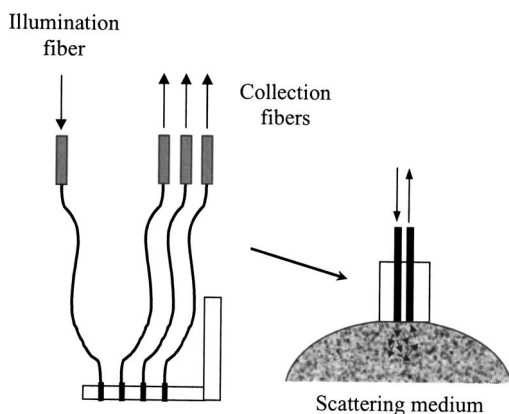


Fig. 3. Schematic of the fiber-optic geometry showing illumination and collection fibers.

ferred to as the light-collection fibers, functioned to collect the light scattered back from the PS suspension. The four fibers were arranged in a linear array, with the illumination fiber first, and with center-to-center spacing of $560\ \mu\text{m}$ for all fibers. The collection fibers will be referred to as collection fibers 2, 3, and 4 starting with fiber 2 adjacent to the illumination fiber, as shown in Fig. 3.

Light-scattering signals corresponding to all three laser wavelengths were measured simultaneously by coupling the desired collection fiber to an integrated spectrometer/detector unit (Ocean Optics S2000, Dunedin, Florida). The detector was a 2048-element linear CCD array, and the overall system had an optical resolution of approximately $0.7\ \text{nm}$ and an effective dispersion of $0.13\ \text{nm}/\text{pixel}$. The spectrometer/detector was controlled by software, and an integration time of $100\ \text{ms}$ was used for the PS study.

PS suspensions were created using monodisperse $7.20\ \mu\text{m}$ -diameter ($0.07\ \mu\text{m}$ standard deviation) PS microspheres (Bangs Laboratories, Inc.). The microspheres were purchased as liquid suspensions with 10% solid content by weight and a density of $1.062\ \text{g}/\text{ml}$. The PS particle size was selected based on a study done by Fantès *et al.* that presented corneal light-scattering analysis as modeled by keratocytes, including size and the number density of the keratocytes at various postoperative times following laser refractive surgery.²⁷ Based on their reported keratocyte density values, the corresponding mean particle-to-particle path lengths were calculated to be on the order of $10\ \mu\text{m}$ for moderate to severe corneal haze. Based on these estimates, the original PS stock suspensions were diluted with ultrapurified deionized water to create four different particle concentrations, which will be referred to as suspensions C1, C2, C3, and C4, where C1 was the densest suspension and C4 was the least dense suspension. In order to evaluate actual suspension particle concentrations, the extinction coefficients were measured using the transmission of variously diluted suspensions. The following equation was used to calculate the extinction coefficient:

$$K_{\text{ext}} = \frac{-\ln(\tau)}{L}, \quad (9)$$

where τ is the transmission, and L is the $1\ \text{cm}$ -optical path length. The final extinction coefficients, the particle

number densities, and corresponding mean scattering path lengths (i.e., average distance between particles) are summarized in Table 1.

The mean scattering path length is generally defined as the average distance (i.e., center-to-center) between scattering particles. The mean scattering path length was calculated for each concentration using a spherical volume element centered about each particle such that the volume fraction of each spherical element was unity. The diameter of the volume element was then set equal to the mean scattering path length. All suspensions were prepared in $15\ \text{ml}$ amber glass bottles and stored under refrigeration between experiments. Prior to each measurement, the PS suspensions were removed from storage, vortex mixed, and then sonified for $15\ \text{min}$.

All measurements were carried out by arranging the fiber-optic mount perpendicular to the specimen surface and submerging it directly into the liquid-PS suspension to a depth of $0.5\ \text{mm}$ using a precision vertical translation stage. It was verified that the scattering response was independent of the fiber-optic probe depth for depths up to $5\ \text{mm}$; hence, effects due to the bottom of the sample bottle were insignificant for the actual depth of $0.5\ \text{mm}$, and the suspensions were effectively semi-infinite reservoirs. The PS sample bottle was held in place by a block of aluminum with a hole machined through to fit the sample bottle diameter. The sample holder was painted flat black and black felt was placed under the entire holder to minimize any reflections of light escaping the bottle.

To control for any fluctuations in laser power, or variations in fiber coupling or optical alignment, reference measurements were performed before and after each PS sample measurement using a small block ($2.5\ \text{cm}$ by $2.5\ \text{cm}$ by $1.9\ \text{cm}$ thick) of commercial-grade, ultrahigh-molecular-weight polyethylene (PE). The use of a solid PE block as a diffuse scattering reference standard provides a consistent and intense scattering signal as compared with a liquid-phase reference; in the latter, particles are subject to sedimentation effects and agglomeration. The dimensions of the reference block were sufficiently large that no boundary effects were observed.

While the fiber was immersed directly in the PS suspension to avoid any surface reflection, the reference measurement was performed by bringing the fiber holder in direct contact (normal to the surface) with the PE reference sample. A typical spectrum recorded for a PS suspension and the corresponding PE reference measurement spectrum are shown in Fig. 4. For a given PS measurement, the absolute peak intensity for each scattering wavelength was calculated by subtracting the average

Table 1. Number Density and Mean Scattering Path Length of Polystyrene Suspensions

PS Suspension	K_{ext} (cm^{-1})	Number Density (cm^{-3})	Mean Scattering Path Length (μm)
C1	88.8	9.5×10^7	27.2
C2	43.6	4.7×10^7	34.4
C3	8.69	9.3×10^6	59.0
C4	1.02	1.1×10^6	120.3

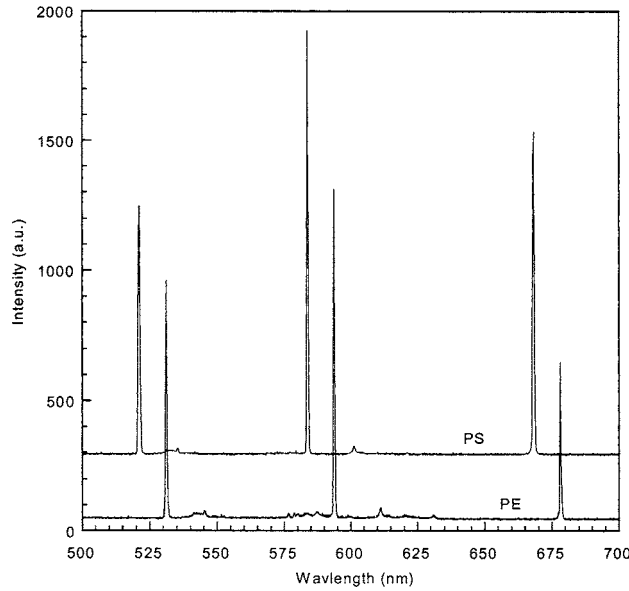


Fig. 4. Representative scattering spectra recorded for PS suspension and PE reference. The PE reference data are two individual spectra recorded before and after the PS suspension measurement. All spectra have the same intensity scale, and the PS spectrum is shifted horizontally for clarity.

baseline intensity and summing the full-width peak area. This was repeated for each wavelength corresponding to the PE reference spectrum. The PS scattering signal at a given wavelength (defined as the PS signal-to-reference ratio) was then calculated by dividing the absolute PS peak area of the PS scattering signal by the average of the two PE reference peak area measurements recorded before and after the PS measurement. The maximum variation of the PE reference signal was less than 10%, with typical deviations much less. The need for absolute signal values during any given experiment was eliminated by using the signal-to-reference ratio; hence the measurements were unaffected by day-to-day changes in laser power or fiber alignment. Measurements were repeated ($N=12$) for each PS suspension concentration, with all replicate measurements recorded on different days.

B. Monte Carlo Simulations

MC simulations were used to support the experimental work by modeling the dense-medium light scattering problem. A FORTRAN-based MC computer code was developed to track individual photons through a simulated dense scattering medium consistent with the PS suspensions, and ultimately to model keratocyte scattering in corneal tissue. The algorithm entails launching a photon into the medium according to an initial azimuthal and a rotational angle, and then tracking the photon in three dimensions in accordance with full Mie light-scattering theory as the photon progresses through the scattering medium. The MC model uses four distinct probability distributions to describe the system, as follows: (1) the initial launch angle α_i , (2) the Mie scattering angle θ , (3) the rotational scattering angle β , and (4) the scattering path length L . The MC scattering geometry is shown schematically in Fig. 5. In addition to light scattering, the absorption of photons between scattering particles was included

in the model by use of a binary probability distribution based on the Beer-Lambert law and the wavelength-dependent absorption coefficient of the scattering medium (e.g., water or tissue).

The probability distribution of the scattering angle ($0^\circ \leq \theta \leq 180^\circ$) was defined based on Mie light-scattering theory. The FORTRAN code DBMie²⁸ was used to generate an array with the vertically and horizontally polarized differential scattering cross sections (σ'_{VV} and σ'_{HH}) corresponding to each integer scattering angle from 0° to 180° for a given scattering particle diameter, wavelength, and refractive indices of the scattering particle and scattering medium. Using the polarization-dependent cross sections, the differential scattering cross section ($\text{cm}^2 \text{sr}^{-1}$) for unpolarized incident light was calculated in accordance with Mie theory as

$$\sigma'_{\text{scat}} = \frac{1}{2}(\sigma'_{VV} + \sigma'_{HH}). \quad (10)$$

By use of the Mie scattering angle distribution array, a probability-based sampling array was constructed. The scattering angle distribution array was first normalized by summing the differential scattering cross sections over all 181 scattering angles and defining the normalization constant as the inverse of this sum. The normalized scattering array was then calculated as the product of each respective cross section and the normalization constant, yielding an output array with each entry an integer value. Due to the high degree of angular dependence with Mie scattering, the range in integer values exceeded seven orders of magnitude, hence numerical precision was important. Finally, a 2D array was defined consisting of the Mie scattering angle and the corresponding normalized integer representative of the scattering cross section.

To randomly sample the Mie scattering distribution, a random number ($0 \leq RND < 1$) was generated and then scaled by the sum of all integers in the 2D Mie scattering angle array. Starting with the first element ($i=0$) of the Mie scattering angle array, a cumulative sum was calcu-

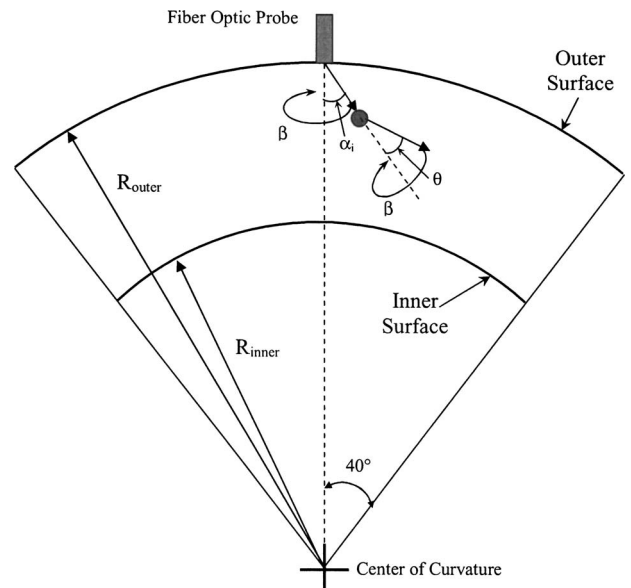


Fig. 5. Scattering geometry for the Monte Carlo simulations.

lated and compared to the scaled random number. The cumulative sum was incremented until the scaled random number was found between the i th and $(i+1)$ th cumulative sums. The corresponding scattering angle of the $(i+1)$ th array element defined the Mie scattering angle for that particular random number. This algorithm has the effect of mapping the Mie scattering angle distribution to a continuous number line, with each linear segment corresponding to a given scattering angle weighted by the respective scattering cross section, and then randomly addressing the number line.

The probability distribution of the initial photon launch angle was based on a Gaussian distribution to model the angular distribution ($-7^\circ \leq \beta \leq +7^\circ$) of light emitted by the optical fiber as defined by its numerical aperture. Because of the relatively smooth monotonic behavior of the Gaussian distribution, a more direct MC sampling algorithm was used than for the Mie scattering angle. For the defined Gaussian distribution, the probability at the limiting angle $P(7^\circ)$ was calculated and a normalization constant was defined as the inverse of this probability. An integer value of the Gaussian distribution was then defined for each launch angle as the product of the Gaussian probability $P(\alpha_i)$ and the normalization constant, noting that the integer value of the limiting angle was unity. A one-dimensional (1D) probability array was then defined of total length equal to the sum of all integer values from the normalized distribution. Finally, the launch angles of the Gaussian distribution were then sequentially written into the 1D array a number of times equal to their normalization value. For example, the limiting angles were written into the final array exactly once. To randomly sample a launch angle, a random number was generated and scaled to the sum of all integer values (i.e., the total array length) as defined above. This scaled value was then converted to an integer and used as the index for the 1D probability array, which then defined the launch angle.

This same procedure was repeated to develop the MC algorithm for selecting the scattering path length. However, the Gaussian distribution was replaced by a lognormal distribution to reflect only positive scattering path lengths and to provide a skewed distribution more indicative of the expected natural distribution of scattering path lengths.

The final element of the overall MC scattering algorithm was the treatment of absorption between two scattering particles. While the scattering medium for the PS suspension experiments was water, with minimal absorption in the visible spectrum (as quantified below), the model was formulated to account for any degree of absorption. The model input was the absorption coefficient K_{abs} (cm^{-1}) of the scattering medium for each wavelength of interest. For each randomly selected scattering path length, a value of transmission τ was defined based on the Beer-Lambert law, namely

$$\tau = \exp(-K_{abs}L), \quad (11)$$

where L is the scattering path length. A random number ($0 \leq RND < 1$) was then generated, and if the random number were less than τ , the photon was passed to the next scattering particle. If the random number exceeded

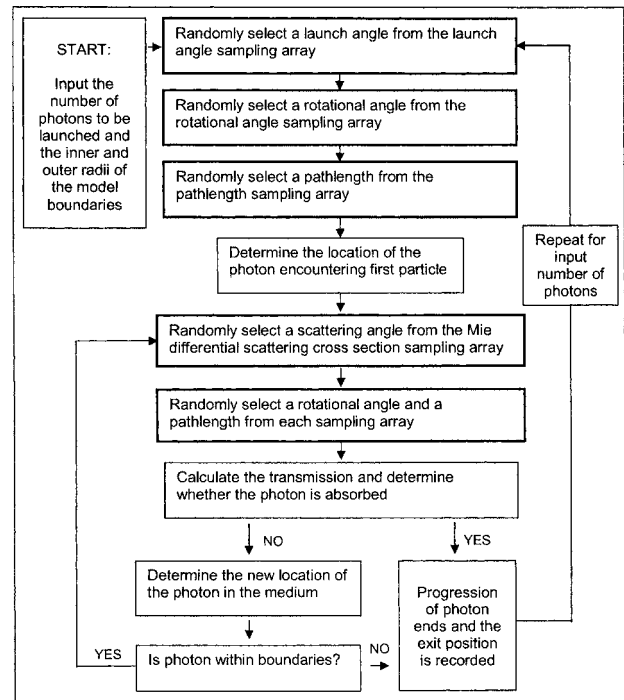


Fig. 6. Flow chart of Monte Carlo program algorithm. Bold boxes represent MC processes.

τ , then the track of that particular photon was terminated. The schematic flowcharts of the MC dense-medium scattering program are shown in Fig. 6.

The MC simulation geometry was designed primarily to model dense-medium scattering associated with corneal tissue, hence a spherical coordinate system was used. The total scattering volume was the annular region defined by two spherical surfaces of radii r_{outer} and r_{inner} as shown in Fig. 5. Simulated photons were launched at the apex of the outer surface and tracked until they exited either the outer surface or the inner surface, or exited the side of the annular region defined by a solid cone of half-angle 40° . The exact position was recorded for all photons that exited the outer surface (i.e., launch surface).

5. RESULTS

A. Polystyrene Suspension Experiments

For all three scattering wavelengths and collection fibers, the scattering signal-to-reference ratio (PS-to-PE) increased as the particle concentration of the PS suspension increased (i.e., with decreasing scattering path length). Figure 7 presents the resulting signal-to-reference values as a function of scattering path length for the three scattering wavelengths of 532, 594, and 670 nm as collected using fiber 2. The scattering signals reveal a marked increase in signal response at the reduced mean scattering path length values. This is indicative of the increasing role of multiple scattering, which yields a nonlinear scattering response with respect to particle concentration, as the PS particle number density increases. Similar trends were observed for collection fibers 3 and 4.

The two-color scattering ratios (532/594, 532/670, and 594/670) were calculated as a function of mean scattering path length for all three collection fibers. The two-color

ratio is defined as the signal-to-reference ratio at the lower wavelength divided by the signal-to-reference ratio at the higher wavelength. The two-color scattering ratio increased with increasing scattering particle concentration (i.e., with increased light scattering) for all three wavelength ratios and all three collection fibers. Figure 8 shows the resulting two-color ratio values for the laser wavelength combination of 594 nm/670 nm and for collection fiber 2. Similar trends were observed for other wavelength combinations and collection fibers, demonstrating the unique signal response of this parameter for the current range of dense-scattering-medium conditions. How-

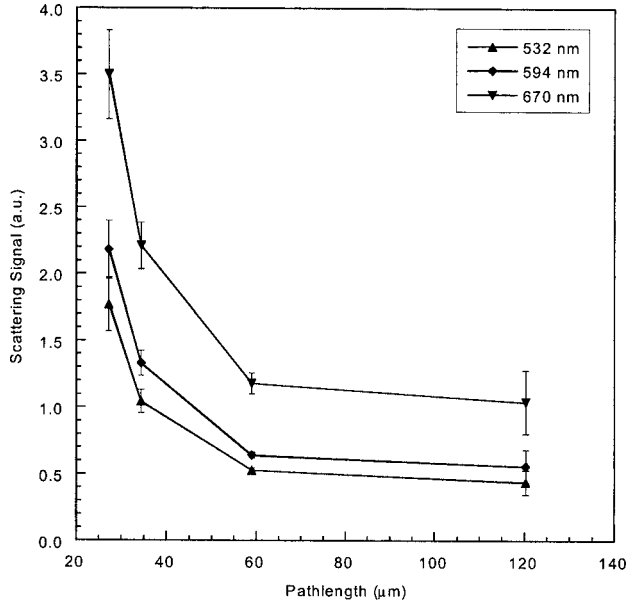


Fig. 7. PS suspension scattering response (PS signal-to-PE reference) as a function of mean scattering path length for the three scattering wavelengths of 532, 594, and 670 nm at fiber 2. The error bars denote \pm one standard deviation ($N=12$).

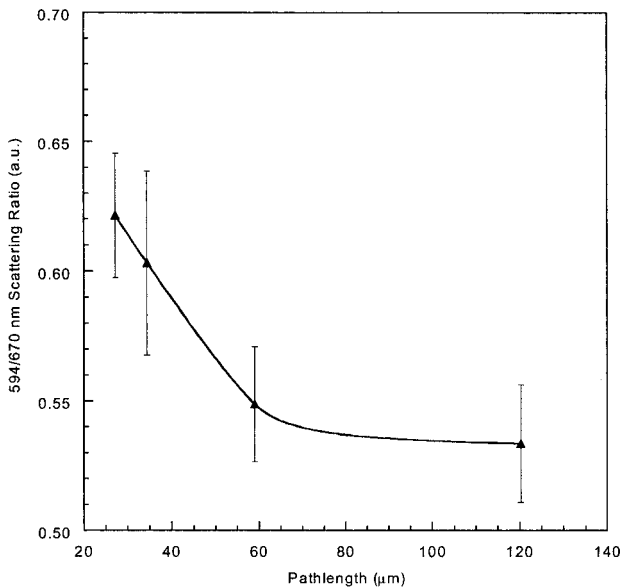


Fig. 8. PS suspension two-color scattering ratio for the laser wavelength combination of 594/670 nm for fiber 2. The error bars denote \pm one standard deviation ($N=12$).

ever, as a metric for changes in scattering particle density, the 594/670 two-color ratio demonstrated a slightly better response (i.e., slope) than the other two-color ratios to changing particle concentration; hence subsequent data analysis will focus on this particular ratio. Essentially, by using the ratio of two unique scattering wavelength signals that are each in turn a ratio of the PS scattering response to the PE reference response, there is no need for any absolute signal calibration. Furthermore, because the laser light is launched through the illumination fiber and subsequently gathered through the separate collection fiber, any direct *surface* reflectance of the input light back into the illumination fiber is inconsequential with respect to the measured scattered light, keeping in mind that light can reach the collection fiber only after undergoing at least one scattering event with a PS particle. With this configuration, surface reflections are eliminated from the collection optics.

While the data presented in Fig. 8 are representative of the two-color scattering response for the PS suspensions, they differ from the absolute PS two-color ratio by a constant value. Specifically, the measured two-color ratios as presented in Fig. 8 are actually the product of the two-color ratio of the PS scattering suspension divided by the two-color ratio of the PE reference sample, as shown by

$$R_{\text{exp}} = \left(\frac{C_{\lambda 1}}{C_{\lambda 2}} \right)_{PS} \left(\frac{C'_{\lambda 2}}{C'_{\lambda 1}} \right)_{PE}, \quad (12)$$

where $(C_{\lambda 1}/C_{\lambda 2})_{PS}$ represents the true two-color scattering ratio for the PS suspension, and $(C'_{\lambda 1}/C'_{\lambda 2})_{PE}$ represents the two-color scattering ratio for the PE reference material.

For all experiments, the absolute scattering signal at a given wavelength S_{λ} may be defined as

$$S_{\lambda} = I_{\lambda} C_{\lambda} \rho_{\lambda} \eta_{\lambda}, \quad (13)$$

where I_{λ} is the incident laser intensity (i.e., from the illumination fiber); C_{λ} is the scattering system coefficient dependent on the effective scattering cross section, scattering particle number density, and degree of multiple scattering; ρ_{λ} is the efficiency of photons entering and exiting the medium (i.e., it accounts for Fresnel surface loss); and η_{λ} is the efficiency and instrument function of the fiber-optic and spectrometer system (i.e., it accounts for surface coupling efficiency, transmission losses, quantum efficiency, and spectrometer dispersion effects). Using this model, the two-color ratio (R) of the PS suspension and the PE reference material, respectively, is defined as

$$R_{PS} = \frac{S_{\lambda 1}}{S_{\lambda 2}} = \frac{I_{\lambda 1} C_{\lambda 1} \rho_{\lambda 1} \eta_{\lambda 1}}{I_{\lambda 2} C_{\lambda 2} \rho_{\lambda 2} \eta_{\lambda 2}}, \quad (14)$$

$$R_{PE} = \frac{S_{\lambda 1}}{S_{\lambda 2}} = \frac{I'_{\lambda 1} \cdot C'_{\lambda 1} \cdot \rho'_{\lambda 1} \cdot \eta'_{\lambda 1}}{I'_{\lambda 2} \cdot C'_{\lambda 2} \cdot \rho'_{\lambda 2} \cdot \eta'_{\lambda 2}}. \quad (15)$$

Based on the experimental methodology, these ratios are related to the measured two-color ratio (PS-to-PE) as follows

Table 2. Two-Color Scattering Calibration Factors for Polyethylene Reference

$C'_{\lambda_2}/C'_{\lambda_1}$	Fiber 2	Fiber 3	Fiber 4
594/532	0.70	0.67	0.65
670/594	0.62	0.62	0.62
670/532	0.43	0.42	0.41

$$R_{\text{exp}} = \frac{R_{PS}}{R_{PE}} = \frac{I_{\lambda_1} I'_{\lambda_2} C_{\lambda_1} C'_{\lambda_2} \rho_{\lambda_1} \rho'_{\lambda_2} \eta_{\lambda_1} \eta'_{\lambda_2}}{I_{\lambda_2} I'_{\lambda_1} C_{\lambda_2} C'_{\lambda_1} \rho_{\lambda_2} \rho'_{\lambda_1} \eta_{\lambda_2} \eta'_{\lambda_1}}. \quad (16)$$

Equation (16) can be simplified by assuming that the laser power is constant over the course of a single experiment ($I_{\lambda_1} \approx I'_{\lambda_1}; I_{\lambda_2} \approx I'_{\lambda_2}$) and that the fiber input and output efficiencies are constant over the wavelength range from 532 to 670 nm (i.e., they have similar Fresnel losses); hence

$$\frac{\rho_{\lambda_1}}{\rho_{\lambda_2}} \approx \frac{\rho'_{\lambda_2}}{\rho'_{\lambda_1}} \approx 1. \quad (17)$$

In addition, the instrument function and wavelength response is independent of the scattering signal source; hence

$$\eta_{\lambda_1} = \eta'_{\lambda_1} \text{ and } \eta_{\lambda_2} = \eta'_{\lambda_2}. \quad (18)$$

Based on these assumptions, the experimental two-color ratio is reduced to the form of Eq. (12). The two-color ratio of the PE reference material ($C'_{\lambda_1}/C'_{\lambda_2}$)_{PE} was calibrated using the following procedure to enable conversion of the measured two-color ratios to an actual two-color scattering response of the PS suspension system. The two-color scattering response of the PE reference material based on Eq. (13) and the above assumptions is given by

$$R_{PE} = \frac{S'_{\lambda_1}}{S'_{\lambda_2}} = \frac{I'_{\lambda_1} C'_{\lambda_1} \eta'_{\lambda_1}}{I'_{\lambda_2} C'_{\lambda_2} \eta'_{\lambda_2}}; \quad (19)$$

hence, the desired calibration parameter is reduced to

$$\frac{C'_{\lambda_2}}{C'_{\lambda_1}} = \frac{S'_{\lambda_2} I'_{\lambda_1} \eta_{\lambda_1}}{S'_{\lambda_1} I'_{\lambda_2} \eta_{\lambda_2}}. \quad (20)$$

For the PE calibration experiments, the two-color signal ratio ($S'_{\lambda_2}/S'_{\lambda_1}$)_{PE} was recorded directly for each of the three wavelength combinations, and the laser power ratio ($I'_{\lambda_1}/I'_{\lambda_2}$)_{PE} was directly measured at the illumination fiber exit using a sensitive power meter. Finally, the instrument response was directly measured using a calibrated blackbody source:

$$\frac{\eta_{\lambda_1}}{\eta_{\lambda_2}} = \frac{S_{B\lambda_1} I_{B\lambda_2}}{S_{B\lambda_2} I_{B\lambda_1}}, \quad (21)$$

where $S_{B\lambda_1}$ and $S_{B\lambda_2}$ are the signals recorded with the blackbody source, and $I_{B\lambda_1}$ and $I_{B\lambda_2}$ are the calibrated blackbody emissive powers. Combining these measurements, the PE two-color response was directly calculated as

$$\left(\frac{C'_{\lambda_2}}{C'_{\lambda_1}} \right)_{PE} = \left(\frac{S'_{\lambda_2} I'_{\lambda_1}}{S'_{\lambda_1} I'_{\lambda_2}} \right) \left(\frac{S_{B\lambda_1} I_{B\lambda_2}}{S_{B\lambda_2} I_{B\lambda_1}} \right). \quad (22)$$

The PE response constants are presented in Table 2 for all three two-color ratios.

B. Monte Carlo Simulations of Polystyrene Suspensions

To corroborate the multicolor scattering response under dense-scattering-medium conditions, the PS suspension experiments were simulated with the MC algorithm described above. The MC simulation geometry was specified to correspond to the geometry of the actual PS suspension experiments, as described below, thereby enabling calculation of the total numbers of simulated photons exiting the input surface (i.e., backscatter) at positions corresponding to fibers 2, 3, and 4. For the PS suspension simulations, the scattering particle input values were a relative refractive index of $m = 1.20 - 0.00i$ based on PS in water ($n = 1.59/1.33$), and a particle diameter of $7.20 \mu\text{m}$.²⁹ The scattering medium was modeled as water with a refractive index of 1.33 and with wavelength-specific absorption coefficients equal to $4.4 \times 10^{-8} \mu\text{m}^{-1}$ at 532 nm, $1.6 \times 10^{-7} \mu\text{m}^{-1}$ at 594 nm, and $4.0 \times 10^{-7} \mu\text{m}^{-1}$ at 670 nm.³⁰

All of the MC sampling distribution algorithms were evaluated individually to confirm that they reproduced the input distribution functions for a large random sample. For the Mie scattering angle distribution, the sampling algorithm was randomly accessed 10^8 times for the input values corresponding to the PS simulations. Figure 9 shows the resulting Mie differential scattering distribution at 594 nm resulting from the MC simulation and the exact differential scattering cross sections as based on Mie theory. The resonant structure characteristic of Mie scattering is apparent in the figure for both the

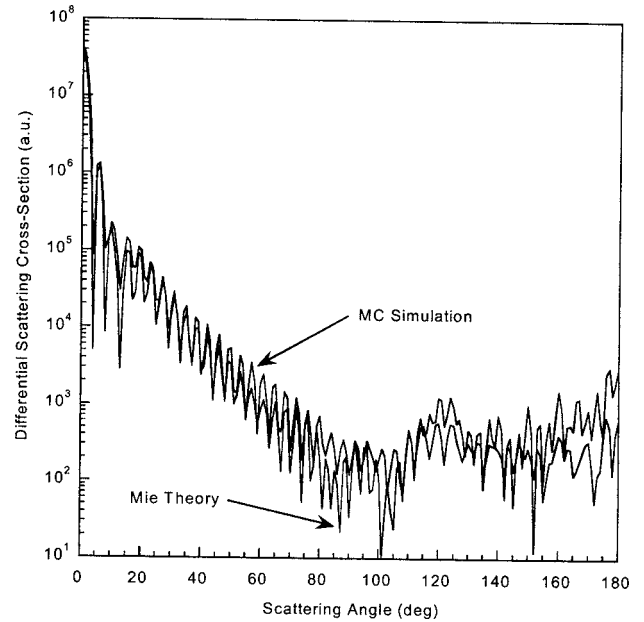


Fig. 9. Comparison of the calculated Mie angular scattering distribution (Mie theory) with the resulting MC sampling algorithm results based on 10^8 trials (MC simulation) for a 594 nm wavelength and a PS particle diameter of $7.2 \mu\text{m}$.

Mie calculations and the MC simulations. In addition, the nearly seven-orders-of-magnitude variation in the differential cross section is noted, with the forward scattering prominent as expected for particles well within the Mie regime ($d \gg \lambda$). The scattering distribution generated by the MC simulation accurately represents the differential scattering cross section distribution per Mie theory. For all four distribution functions, the MC sampling algorithms were verified and in all cases accurately reproduced the input sampling functions.

To simulate the geometry of the PS suspensions, the outer radius in the MC scattering geometry was increased to 20 mm and the inner radius was reduced to 10 mm, providing an effective suspension depth of 10 mm. By varying the depth of the suspension ($\text{depth} = r_{\text{outer}} - r_{\text{inner}}$), it was determined that the number of photons exiting the outer surface (i.e., backscattered photons) converged by a depth of 10 mm. This can be interpreted as the maximum penetration depth for backscattered photons for the range of particle concentrations and scattering parameters, meaning that the probability of a photon penetrating to a depth of 10 mm and then being scattered back to the outer surface was converging to zero. Setting the inner boundary to a finite value in this manner significantly reduced the computational time as compared with letting the photons continue to travel to greater depths, and accurately modeled the finite depth of the glass vials used for the actual PS experiments.

Using the conditions described above, MC simulations were performed to simulate the dense-medium scattering realized in the PS suspension experiments. Each simulation was performed by launching 10^7 photons and calculating the resulting distribution of photons that exited the outer surface (i.e., front surface). Simulations were performed for wavelengths of 532, 594, and 670 nm, and for corresponding mean path lengths of 27.2, 34.4, 59, and 120.3 μm , which correspond to the conditions of the PS suspension experiments. Through replicate simulations, the total number of photons used was determined to be sufficient to provide highly reproducible results. Typical run times using the FORTRAN code on a 2 GHz PC platform was in the range of 10 h.

For the MC simulation conditions corresponding to a mean path length of 120.3 μm and all three scattering wavelengths, 44.0% to 59.5% of the launched photons exited through the rear boundary, 13.8% to 22.6% through the front boundary (i.e., front surface via backscatter), 26.7% to 33.2% through a side boundary, and 0.06% to 0.51% of the incident photons were absorbed within the medium. For the 27.2 μm path length, the range over the three wavelengths was 11.2% to 16.5% of the launched photons exiting through the rear boundary, 52.5% to 66.4% through the front boundary, 22.1% to 30.9% through a side boundary, and 0.11% to 0.7% of total photons were absorbed in the medium. For the intermediate path lengths of 34.4 and 59 μm , similar results were obtained. In all cases, the largest percentage of photons scattered to the front surface corresponded to the wavelength of 594 nm, while the largest percentage of photons scattered to the back surface corresponded to the 532 nm wavelength.

For each wavelength and scattering concentration, the

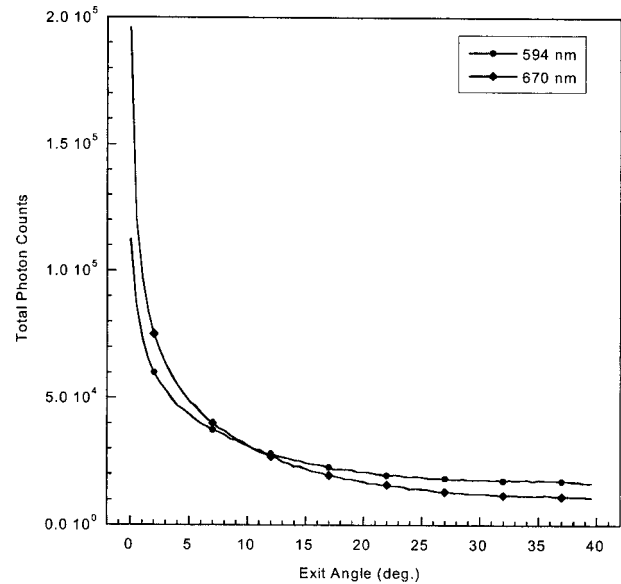


Fig. 10. Angular distribution of front-exiting photons based on 10^7 MC trials for scattering wavelengths of 594 and 670 nm. The mean scattering path length is 27.2 μm .

angular distribution of photons scattered from the front surface was recorded. Figure 10 shows the angular distribution of backscattered photons for the mean scattering path length of 27.2 μm corresponding to the two incident wavelengths of 594 nm and 670 nm. The average number of scattering events for a front-exiting photon was 499 for the pathlength of 27.2 μm , corresponding to all angles of collection. Note that the angular positions of 4°, 8°, and 12° correspond to the positions of fibers 2, 3, and 4, respectively. For these three fiber positions, the average number of scattering events per exiting photon was 287 for fiber 2, 429 for fiber 3, and 530 for fiber 4, which correspond to average total travel distances of 7.8, 11.7, and 14.4 mm, respectively, based on the mean free paths. The typical backscattered photon may be considered to travel within a spherical volume of radius equal to half these distances, or on the order of 6 mm, which is less than the total 10 mm depth of the model geometry.

Several trends are apparent in the MC simulation results. Overall, as the suspension concentration was increased (i.e., decreasing mean scattering path length), the percentage of launched photons exiting through the front boundary via backscattering increased, while the percentage of photons exiting through the rear boundary via forwardscattering decreased. The MC simulation response was consistent with that observed in the actual PS suspension experiments. With regard to the backscattered photons, the greatest numbers of backscattered photons were recorded at a position corresponding to the point of photon launch; in other words, directly back into the illumination fiber position. There was a monotonic decay in the number of recorded photons as the distance away from the launch point was increased, as seen in Fig. 10. However, the rate of decay was different for the different scattering wavelengths and mean free path lengths, making the two-color ratio a unique metric.

The MC simulations enable direct calculation of the two-color scattering ratio, which is defined as

$$R_{MC} = \frac{E_{\lambda_1}}{E_{\lambda_2}} = \frac{C_{\lambda_1} N_{\lambda_1}}{C_{\lambda_2} N_{\lambda_2}}, \quad (23)$$

where E_{λ} is the number of photons exiting the front surface at a given position and wavelength, C_{λ} represents the overall system scattering coefficient as defined above, and N_{λ} is the total number of photons launched from the illumination optic. Note that the MC simulation employs efficiency coefficients of unity for launching and collection of photons at the representative model interfaces.

To best match the geometry corresponding to the actual PS suspension experiments, the two-color ratios were calculated using collection angles of 4°, 8°, and 12° and a total angular integration of $\pm 0.5^\circ$, which correspond to the angular collection solid angle of fibers 2, 3, and 4, respectively. Using the same number of incident photons for each wavelength, the ratio of $N_{\lambda_1}/N_{\lambda_2}$ reduces to unity, hence the two-color MC simulation ratio can be directly compared to the PS suspension experimental values, once the experimental values have been corrected for the PE response constants listed in Table 2. The MC simulated two-color scattering ratios are presented in Fig. 11, along with the corrected experimental PS suspension two-color ratios for the 594/670 nm ratio corresponding to fiber 2.

The two-color ratios of the PS experimental values are in very good agreement with those of the MC simulations with regard to the overall response curve shape. Moreover, the absolute values of 594/670 nm two-color ratios demonstrate excellent agreement for fiber 2, as seen in the figure, with an average deviation of 2.5%. Similar agreement in shape was obtained with fibers 3 and 4, although a slight offset between the two curves was observed, with the average agreement between the experimental values and MC simulations equal to 10.3% and 15.6% for fibers 3 and 4, respectively. For the 532/594 nm and 532 nm/670 nm ratios, the agreement between the

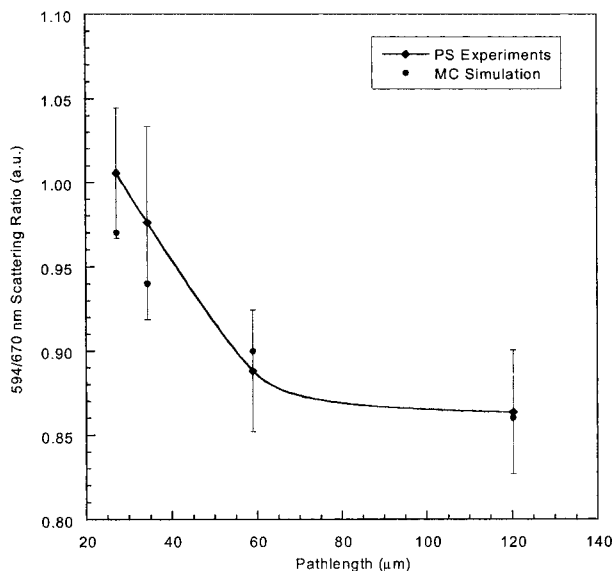


Fig. 11. Comparison of the experimental PS suspension two-color scattering ratios (594/670 nm) with the MC simulations (10^7 trials) as a function of mean scattering path length for fiber 2. The error bars on the experimental values denote \pm one standard deviation ($N=12$).

experimental trends and the MC simulation was also very good, while the degree of absolute agreement was always within a factor of two. It is noted that the PS spheres were modeled as dielectrics (i.e., no absorption), while wavelength-dependent absorption was assigned to the water medium in the simulation. It is suspected that absorption effects at the wavelength of 532 nm were not perfectly matched in the MC simulation, which resulted in an underestimate of 532 nm backscatter. Overall, the MC simulations and the PS suspension experiments demonstrate a unique two-color dependence of light scattering on the overall scattering particle concentrations under these dense-scattering-medium conditions, making the two-color ratio a candidate metric for quantifying the degree of scatterers present. Furthermore, the excellent agreement between the experimental results and MC simulations provides validation of the MC model, thereby supporting the use of the MC code to optimize the two-color response with respect to the collection fiber placement and the specific scattering-wavelength pairs.

C. Monte Carlo Simulations of Corneal Haze

The MC model was adjusted to simulate the geometry of a human cornea to enable assessment of the two-color scattering approach as it responded to changing number density of scattering particles (e.g., keratocytes). The outer radius was set to 8.0 mm, a curvature consistent with human corneal dimensions, and the inner radius was set to 7.3 mm corresponding to a total thickness of 700 μm . Human corneas are typically between 500 to over 600 μm thick in the center (e.g., $616.6 \pm 108.3 \mu\text{m}$ mean thickness in a recent study³¹), thickening to about 650 to 700 μm near the limbus. Scattering centers were modeled as keratocytes with an equivalent spherical diameter of 6.3 μm . The scattering particle refractive index was set to $1.44 - 0.01i$, which provides a relative index of $1.08 - 0.01i$, as based on the analysis by del Val and co-workers.³² It is noted here that the interactions of corneal inflammation, corneal scattering, and the manifestation of corneal haze form a very complex problem (see Refs. 3–5), in which keratocytes may undergo significant remodeling with regard to both shape and optical properties. Furthermore, the overall nature of the extracellular stromal matrix may undergo transformation that may affect the baseline scattering parameters as well.^{33–35}

Clearly the use of Mie scattering theory is a first approximation. Nonetheless, the actual scattering behavior is likewise expected to be characterized by a strong angular behavior and/or resonant structure typical of Mie theory, hence the exploration of the two-color scattering response with the appropriate corneal geometry is a reasonable starting point to assess feasibility of the two-color scattering technique. A range of clinically relevant mean free path lengths was investigated (10 to 60 μm) covering the range of mild to severe haze based on the reported keratocyte densities in monkey corneas following PRK.²⁷ Measurements of keratocyte number densities in normal human corneas have been reported in the range of 20,000 to 24,000 cells/ mm^3 based on confocal microscopy,^{36,37} which corresponds to a mean free path of ≈ 43 to 45 μm . Finally, wavelength-dependent absorption coefficients of 1.45 cm^{-1} at 594 nm and 1.20 cm^{-1} at

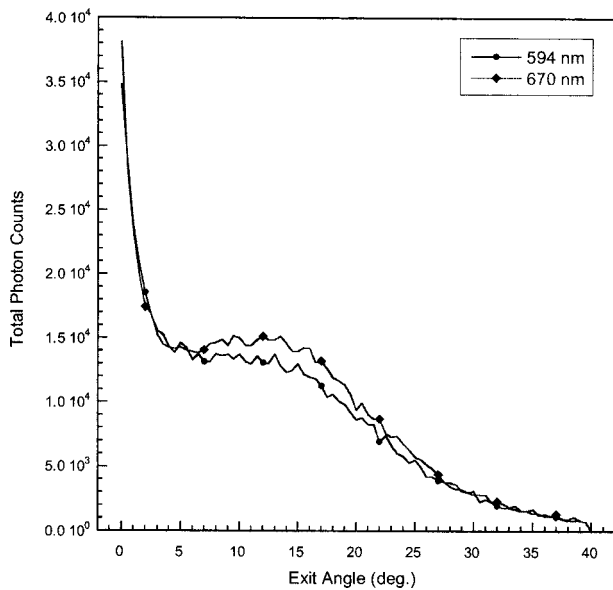


Fig. 12. Angular distribution of front-exiting photons for the corneal tissue model based on 10^7 MC trials for scattering wavelengths of 594 and 670 nm. The mean scattering path length is $15 \mu\text{m}$.

670 nm were used based on values reported for corneal tissue.³⁸ Using this new geometry, 100 to 300 million photons were simulated for both 594 and 670 nm wavelengths over a range of mean scattering path lengths from 10 to $60 \mu\text{m}$. The corresponding scattering number densities range from $\approx 2 \times 10^6 \text{ mm}^{-3}$ for the $10 \mu\text{m}$ mean path to 8800 mm^{-3} for the $60 \mu\text{m}$ pathlength.

For each wavelength and scattering concentration, the angular distribution of photons scattered back to the front surface was recorded. Figure 12 shows the angular distribution of backscattered photons for the mean scattering path length of $15 \mu\text{m}$ corresponding to the two incident wavelengths. The average number of scattering events for a front-exiting photon was 142 for the pathlength of $15 \mu\text{m}$, corresponding to all angles of collection. This value decreased to an average of 35 scattering events for the mean path length of $60 \mu\text{m}$. Clearly, the relatively finite thickness of the model ($700 \mu\text{m}$) limits the depth that may be reached before the photon exits the rear surface of the model. In fact, from 87.7% to 92.0% of the incident photons exited the rear surface over the range of mean scattering path lengths examined. The near total balance of remaining photons exited the front surface, as less than 0.03% were found to exit the side of the model for all conditions. A careful study of the angular distribution for the range of mean scattering paths enabled selection of an optimal region to collect the backscattering light such that the two-color response was maximized for changes in scattering density. Based on this analysis, the optimal point of collection was an angle of 14.5° , which corresponds with the region of maximum difference between the two curves as observed in Fig. 12. For further analysis, the three angular positions of 14° , 14.5° , and 15° were summed to represent placement of the collection fiber at this optimal angular location.

For a fiber position of 14.5° , the average number of scattering events per front-exiting photon was 255 for a

mean path length of $10 \mu\text{m}$, 82 for $30 \mu\text{m}$, and only 40 for a path length of $60 \mu\text{m}$. These correspond to average total travel distances of 2.6, 2.5, and 2.4 mm, respectively. It is noted that the distance along the arc between the photon launch point and the 14.5° collection point is 2.0 mm. If one considers the average travel distance of ~ 2.5 mm for these front-exiting photons, it is interesting that this average value is in close agreement with the total path length defined by any combination of two straight lines, such that the first line originates from the launch point and ends on the inner surface at a point between the launch and collection point, and the second line originates from the terminus point of the first line and ends at the collection point on the outer surface. The result of such a simplification would be that front-exiting photons are launched and travel in a relatively straight path toward the back surface (i.e., dominant forwardscattering) until they undergo a scattering event that abruptly sends them back toward the front surface (i.e., backscattering event). In other words, there is simply insufficient depth ($700 \mu\text{m}$) in the model geometry to enable the incident photons to make a gradual turn back to the front surface. This stands in contrast to the PS simulations, where the average photon travel distance was greater than 14 mm for fiber 4 (12°) with a mean scattering path length of $27.2 \mu\text{m}$.

The differences between the finite-depth corneal geometry and the essentially infinite-depth PS model are expected to be manifest in the two-color scattering ratio as recorded on the front surface. Specifically, the two-color PS results are most likely weighted by differences in *forwardscattering*, as the large effective optical depth leads to an effective integration over all scattering angles, which must be dominated by forwardscattering per the Mie distribution (see Fig. 9). In contrast, the short overall optical path of the corneal simulations coupled with the finite geometry is concluded to depend strongly on the

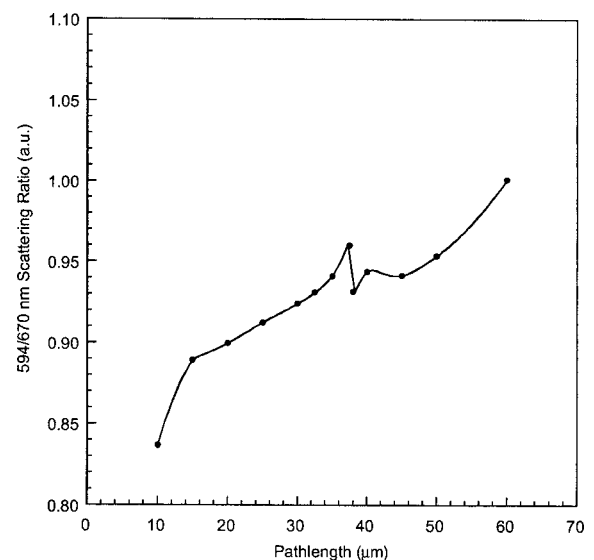


Fig. 13. MC simulation results for the two-color scattering ratio (594/670 nm) corresponding to the corneal scattering geometry and optical properties. Results are for an optimal fiber collection angle of 14.5° and with scattering particle diameter equal to $6.3 \mu\text{m}$.

rather low occurrence of a *backscattering* event, hence backscattering becomes the controlling step. In view of this forwardscattering versus backscattering framework, one might expect a markedly different response in the two-color ratio between the PS and cornea simulations. This is in fact the case, as observed in the two-color scattering ratios presented in Fig. 13 for the corneal model.

Figure 13 demonstrates the uniqueness of the two-color ratio with respect to the scattering particle density, although this relationship gives the inverse behavior with respect to scattering density as was observed with the PS experiments and MC modeling results. While the overall trend follows a monotonic response, it is noted that a unique feature is observed around an optical pathlength of 30 μm , namely, a small kink in the two-color scattering response function. Additional calculations around this point, as well as investigation at other scattering angles, revealed this to be a consistent feature. It is difficult to speculate as to the origin of this feature, but perhaps the response in this region is due to a resonant feature of the Mie distribution coupling to the finite length scales of the corneal geometry and mean free path.

6. CONCLUSIONS

This study was designed to explore the applicability of a two-color light scattering response as applied to quantify the response of dense-medium scattering, namely, PS suspensions and corneal tissue. Overall, the experimental and modeling studies were consistent in the context of multiple Mie scattering in a dense medium, thereby corroborating the two-color approach. It was verified that over a range of collection angles the two-color scattering response increased with increasing scattering particle density in the PS suspension experiments. Furthermore, the results of the MC simulations were in excellent agreement with the observed experimental values for the PS suspension experiments. In concert, the current results demonstrate a unique color dependence of light scattering response under these dense-scattering-medium conditions, enabling data self-normalization through the two-color ratio that is responsive to changes in the concentration of scattering particles. Of further significance to clinical applications, the use of separate illumination and collection fibers in direct contact with the dense-medium surface (e.g., cornea) eliminates any potential effects of surface reflection, hence the response to true *tissue* scattering is isolated and thereby enhanced. Overall, the multicolor scattering techniques show promise for use as a quantitative metric for assessment of dense-medium scattering, including for assessment of corneal haze. Additional experiments, especially with animal models, and more complex modeling of keratocyte and stromal scattering, will be useful for further evaluating this methodology.

ACKNOWLEDGMENTS

The authors thank Greg Schultz (University of Florida) and Michael Goldstein (Tufts University School of Medicine) for bringing the interesting problem of corneal haze to our attention and providing the motivation to pursue

this study. This work was funded in part by the National Science Foundation through grant EEC-0080453. Address correspondence to D.W. Hahn, Box 116300, University of Florida, Gainesville, Florida 32611, or by e-mail to dwhahn@ufl.edu.

REFERENCES

1. G. B. Benedek, "Theory of transparency of the eye," *Appl. Opt.* **10**, 459–473 (1971).
2. T. Nishida, "Cornea, sclera, and ocular adnexa anatomy, biochemistry, physiology and biomechanics," in *Cornea: Fundamentals of Corneal and External Disease*, J. H. Krachmer M. J. Mannis, and E. J. Holland, eds. (Mosby, 1997), pp. 3–27.
3. G. S. Schultz, "Modulation of corneal wound healing," in *Cornea: Fundamentals of Corneal and External Disease*, J. H. Krachmer, M. J. Mannis, and E. J. Holland, eds. (Mosby, 1997), pp. 183–198.
4. T. Moller-Pedersen, H. D. Cavanagh, W. M. Petroll, and J. V. Jester, "Stromal wound healing explains refractive instability and haze development after photorefractive keratectomy—A 1-year confocal microscope study," *Ophthalmology* **107**, 1235–1245 (2000).
5. S. W. Chang, A. Benson, and D. T. Azar, "Corneal light scattering with stromal reformation after laser in situ keratomileusis and photorefractive keratectomy," *J. Cataract Refract. Surg.* **24**, 1064–1069 (1998).
6. C. P. Lohmann, G. T. Timberlake, F. W. Fitzke, D. S. Gartry, M. K. Muir, and J. Marshall, "Corneal light scattering after excimer laser photorefractive keratectomy: The objective measurements of haze," *Refract. Corneal Surg.* **8**, 114–121 (1991).
7. S. Jain, J. M. Khoury, W. Chamon, and D. T. Azar, "Corneal light scattering after laser in situ keratomileusis and photorefractive keratectomy," *Am. J. Ophthalmol.* **120**, 532–534 (1995).
8. R. L. McCally, P. J. Connolly, S. Jain, and D. T. Azar, "Objective measurements of haze following phototherapeutic excimer laser ablation of cornea," *Proc. SPIE* **2126**, 161–165 (1994).
9. R. E. Braunstein, S. Jain, R. L. McCally, W. J. Stark, P. J. Connolly, and D. T. Azar, "Objective measurement of corneal light scattering after excimer laser keratectomy," *Ophthalmology* **103**, 439–443 (1996).
10. H. A. Andrade, M. B. McDonald, J. C. Liu, M. Abdelmegeed, R. Varnell, and G. Sunderland, "Evaluation of an opacity lensometer for determining corneal clarity following excimer laser photoablation," *Refract. Corneal Surg.* **6**, 346–351 (1990).
11. J. Li, J. V. Jester, H. D. Cavanagh, T. D. Black, and W. M. Petroll, "On-line 3-dimensional confocal imaging *in vivo*," *Invest. Ophthalmol. Visual Sci.* **41**, 2945–2953 (2000).
12. W. M. Petroll, J. V. Jester, and H. D. Cavanagh, "Quantitative three-dimensional confocal imaging of the cornea in situ and *in vivo*: System design and calibration," *Scanning* **18**, 45–49 (1996).
13. T. Moller-Pedersen, M. Vogel, H. F. Li, W. M. Petroll, H. D. Cavanagh, and J. V. Jester, "Quantification of stromal thinning, epithelia thickness, and corneal haze after photorefractive keratectomy using *in vivo* confocal microscopy," *Ophthalmology* **104**, 360–368 (1997).
14. L. H. Wang and S. L. Jacques, "Hybrid model of Monte Carlo simulation and diffusion theory for light reflectance by turbid media," *J. Opt. Soc. Am. A* **10**, 1746–1752 (1993).
15. L. H. Wang, S. L. Jacques, and L. Q. Zheng, "MCML—Monte Carlo modeling of light transport in multi-layered tissues," *Comput. Methods Programs Biomed.* **47**, 131–146 (1995).
16. H. Key, E. R. Davies, P. C. Jackson, and P. N. T. Wells, "Monte Carlo modeling of light propagation in breast tissue," *Phys. Med. Biol.* **36**, 591–602 (1991).
17. S. Bartel and A. H. Hielscher, "Monte Carlo simulations of

- the diffuse backscattering Mueller matrix for highly scattering media," *Appl. Opt.* **39**, 1580–1588 (2000).
18. A. Sassaroli, C. Blumetti, F. Martelli, L. Alianelli, D. Contini, A. Ismaelli, and G. Zaccanti, "Monte Carlo procedure for investigating light propagation and imaging of highly scattering media," *Appl. Opt.* **37**, 7392–7400 (1998).
 19. M. H. Koelink, F. F. M. de Mul, J. Greve, R. Graaff, A. C. M. Dassel, and J. G. Aarnoudse, "Laser Doppler blood flowmetry using two wavelengths: Monte Carlo simulations and measurements," *Appl. Opt.* **33**, 3549–3558 (1994).
 20. A. Kienle, M. S. Patterson, L. Ott, and R. Steiner, "Determination of the scattering coefficient and the anisotropy factor from laser Doppler spectra of liquids including blood," *Appl. Opt.* **35**, 3404–3412 (1996).
 21. B. Kaplan, G. Ledanois, and B. Drevillon, "Mueller matrix of dense polystyrene latex sphere suspensions: Measurements and Monte Carlo simulation," *Appl. Opt.* **40**, 2769–2777 (2001).
 22. B. W. Pogue and G. Burke, "Fiber-optic bundle design for quantitative fluorescence measurement from tissue," *Appl. Opt.* **37**, 7429–7436 (1998).
 23. M. Kerker, "Scattering by a sphere," in *The Scattering of Light and Other Electromagnetic Radiation*, E. M. Loebel, ed. (Academic, 1969), pp. 42–50.
 24. H. C. van de Hulst, "Rigorous scattering theory for spheres of arbitrary size," in *Light Scattering by Small Particles* (Dover, 1981), Chap. 9, pp. 114–130.
 25. C. F. Bohren and D. R. Huffman, *Absorption and Scattering of Light by Small Particles* (Wiley Science Paperback Series, 1998).
 26. A. R. Jones, "Scattering of electromagnetic radiation in particulate laden fluids," *Prog. Energy Combust. Sci.* **5**, 73–96 (1979).
 27. F. E. Fantes, K. D. Hanna, G. O. Waring III, Y. Pouliquen, K. P. Thompson, and M. Savoldelli, "Wound healing after excimer laser keratomileusis (photorefractive keratectomy) in monkeys," *Arch. Ophthalmol.* (Chicago) **108**, 665–675 (1990).
 28. J. V. Dave, "Subroutines for computing the parameters of the electromagnetic radiation scattered by a sphere," IBM Corp. Report 320–3237 (May 1968).
 29. *CRC Handbook of Chemistry and Physics*, R. C. Weast, ed. (CRC Press, 1980).
 30. G. M. Hale and M. R. Querry, "Optical constants of water in the 200 nm to 200 μm wavelength region," *Appl. Opt.* **12**, 555–563 (1973).
 31. J. B. Jonas and L. Holbach, "Central corneal thickness and thickness of the lamina cribrosa in human eyes," *Invest. Ophthalmol. Visual Sci.* **46**, 1275–1279 (2005).
 32. J. A. del Val, S. Barrero, B. Yanez, J. Merayo, J. A. Aparicio, V. R. Gonzalez, J. C. Pastor, and S. Mar, "Experimental measurement of corneal haze after excimer laser keratectomy," *Appl. Opt.* **40**, 1727–1734 (2001).
 33. R. L. McCally and R. A. Farrell, "Structural implications of small-angle light-scattering from cornea," *Exp. Eye Res.* **34**, 99–113 (1982).
 34. D. E. Freund, R. L. McCally, and R. A. Farrell, "Direct summation of fields for light-scattering by fibrils with applications to normal corneas," *Appl. Opt.* **25**, 2739–2746 (1986).
 35. D. E. Freund, R. L. McCally, R. A. Farrell, S. M. Cristol, N. L. Lhernault, and H. F. Edelhauser, "Ultrastructure in anterior and posterior stroma of perfused human and rabbit corneas—Relation to transparency," *Invest. Ophthalmol. Visual Sci.* **36**, 1508–1523 (1995).
 36. J. W. McLaren, C. B. Nau, A. S. Kitzmann, and W. M. Bourne, "Keratocyte density: Comparison of two confocal microscopes," *Invest. Ophthalmol. Visual Sci.* **45**, E-Abstract 152 (2004).
 37. S. V. Patel, J. W. McLaren, D. O. Hodge, and W. M. Bourne, "Normal human keratocyte density and corneal thickness measurement by using confocal microscopy *in vivo*," *Invest. Ophthalmol. Visual Sci.* **42**, 333–339 (2001).
 38. J. Eichler and T. Seiler, *Lasertechnik in der Medizin* (Springer-Verlag, 1991).